nature communications

Article

https://doi.org/10.1038/s41467-024-51619-9

Harnessing forward multiple scattering for optical imaging deep inside an opaque medium

Received: 5 June 2024

Accepted: 14 August 2024

Published online: 27 August 2024

Check for updates

Ulysse Najar[1], Victor Barolle[1], Paul Balondrade[1], Mathias Fink[1], Claude Boccara[1] & Alexandre Aubry[1]

As light travels through a disordered medium such as biological tissues, it undergoes multiple scattering events. This phenomenon is detrimental to in-depth optical microscopy, as it causes a drastic degradation of contrast, resolution and brightness of the resulting image beyond a few scattering mean free paths. However, the information about the inner reflectivity of the sample is not lost; only scrambled. To recover this information, a matrix approach of optical imaging can be fruitful. Here, we report on a de-scanned measurement of a high-dimension reflection matrix **R** via low coherence interferometry. Then, we show how a set of independent focusing laws can be extracted for each medium voxel through an iterative multi-scale analysis of wave distortions contained in **R**. It enables an optimal and local compensation of forward multiple scattering paths and provides a three-dimensional confocal image of the sample as the latter one had become digitally transparent. The proof-of-concept experiment is performed on a human opaque cornea and an extension of the penetration depth by a factor five is demonstrated compared to the state-of-the-art.

Multiple scattering of waves concerns many domains of physics, ranging from optics or acoustics to solid-state physics, seismology, medical imaging, or telecommunications. In an inhomogeneous medium where the refractive index n depends on the spatial coordinates $\mathbf{r}$, several physical parameters are relevant to characterize wave propagation: (i) the scattering mean free path ℓ_s, which is the average distance between two successive scattering events; (ii) the transport mean free path ℓ_t, which is the distance after which the wave has lost the memory of its initial direction. For a penetration depth z smaller than ℓ_s, ballistic light is predominant and standard focusing methods can be employed; for $z > \ell_s$, multiple scattering events result in a gradual randomization of the propagation direction before reaching the diffusive regime for $z > \ell_t$. Although it gives rise to fascinating interference phenomena such as perfect transmission[1,2] or Anderson localization[3,4], multiple scattering still represents a major obstacle to deep imaging and focusing of light inside complex media[5,6].

To cope with the fundamental issue of multiple scattering, several approaches have been proposed to enhance the single scattering contribution drowned into a predominant diffuse background[5,7,8]. One solution is to perform a confocal discrimination and coherent time gating of singly-scattered photons by means of interferometry. This is the principle of optical coherence tomography[9], equivalent to ultrasound imaging for light. Nevertheless, a lot of photons associated with distorted trajectories are rejected by the confocal filter while they still contain a coherent information on the medium reflectivity. Originally developed in astronomy[10], adaptive optics (AO) has been transposed to optical microscopy in order to address this issue[11]. Nevertheless, it only compensates for low-order aberrations induced by long-scale fluctuations of the optical index and does not address high-order aberrations generated by forward multiple scattering events. To circumvent the latter problem, one has to go beyond a confocal scheme and investigate the cross-talk between the pixels of the image. This is

[1]Institut Langevin, ESPCI Paris, PSL University, CNRS, 75005 Paris, France. e-mail: alexandre.aubry@espci.fr

the principle of matrix imaging in which the relation between input and output wave-fields is investigated under a matrix formalism.

While a subsequent amount of work has considered the transmission matrix **T** for optimizing wave control and focusing through complex media[12–17], this configuration is not the most relevant for imaging purposes since only one side of the medium is accessible for most in-vivo applications. Moreover, in all the aforementioned works, the scattering medium is usually considered as a black box, while imaging requires to open it. To that aim, a reflection matrix approach of wave imaging (RMI) has been developed for the last few years[18–21]. The objective is to determine, from the reflection matrix **R**, the **T**-matrix between sensors outside the medium and voxels mapping the sample[22]. Proof-of-concept studies have reported penetration depths ranging from $7\ell_s$[23] to $10\ell_s$[19] but the object to image was a resolution target whose strong reflectivity artificially extends the penetration depth by several ℓ_s compared with direct tissue imaging[8]. Follow-up studies also considered the imaging of highly reflecting structures (e.g. myelin fibers) through an aberrating layer (e.g mouse skull)[20], in a wavelength range that limits scattering and aberration from tissues[24]. On the contrary, here, we want to address the extremely challenging case of three-dimensional imaging of biological tissues themselves (cells, collagen, extracellular matrix etc.) at large penetration depth (z ~ $10\ell_s$), regime in which aberration and scattering effects are spatially-distributed over multiple length-scales.

Inspired by previous works[25,26], full-field optical coherence tomography (FFOCT)[27,28] will be used here to record the **R** − matrix. In FFOCT, the incident wave-field is temporally- and spatially-incoherent. It enables, by means of low coherence interferometry, a parallel acquisition of a time-gated confocal image[29] at a much better signal-to-noise ratio than a traditional point scanning scheme for equal measurement time and power[30]. By splitting the incident wave-field into two laterally-shifted components, a de-scanned measurement of **R** can be performed without a tedious raster scanning of the field-of-view[20].

Another advantage of the de-scanned basis is the direct access to the distortion matrix **D** through a Fourier transform. This matrix basically connects any focusing point with the distorted part of the associated reflected wavefront[19,21]. A multi-scale analysis of **D** is here proposed to estimate the forward multiple scattering component of the **T**-matrix at an unprecedented spatial resolution (~ 6 μm). Once the latter matrix is known, one can actually unscramble, in post-processing, all wave distortions and multiple scattering events undergone by the incident and reflected waves for each voxel. A three-dimensional confocal image of the medium can then be retrieved as if the medium had been made digitally transparent.

The experimental proof-of-concept presented in this paper is performed on a human ex-vivo cornea that we chose deliberately to be extremely opaque. Its overall thickness is of $10\ell_s$. FFOCT shows an imaging depth limit of $2\ell_s$ due to aberration and scattering. Strikingly, RMI enables to recover a full 3D image of the cornea at a resolution close to $\lambda/4$ (~ 230 nm) and a penetration depth enhanced by, at least, a factor five.

Results

Measuring a de-scan reflection matrix

Our approach is based on a de-scanned measurement of the time-gated reflection matrix **R** from the scattering sample. Inspired by time-domain FFOCT[27,28], the corresponding set up is displayed in Fig. 1a. It consists in a Michelson interferometer with microscope objectives in both arms (Fig. 1a). In the first arm, a reference mirror is placed in the focal plane of a microscope objective (MO). The second arm contains the scattering sample to be imaged. Because of the broad spectrum of the incident light, interferences occur between the two arms provided that the optical path difference through the interferometer is close to zero. The length of the reference arm determines the slice of the sample (coherence volume) to be imaged and is adjusted in order to match with the focal plane of the MO in the sample arm. The back-scattered light from each voxel of the coherence volume can only interfere with the light coming from the conjugated point of a reference mirror. The spatial incoherence of the light source actually acts as a physical confocal pinhole (Fig. 1c). All these interference signals are

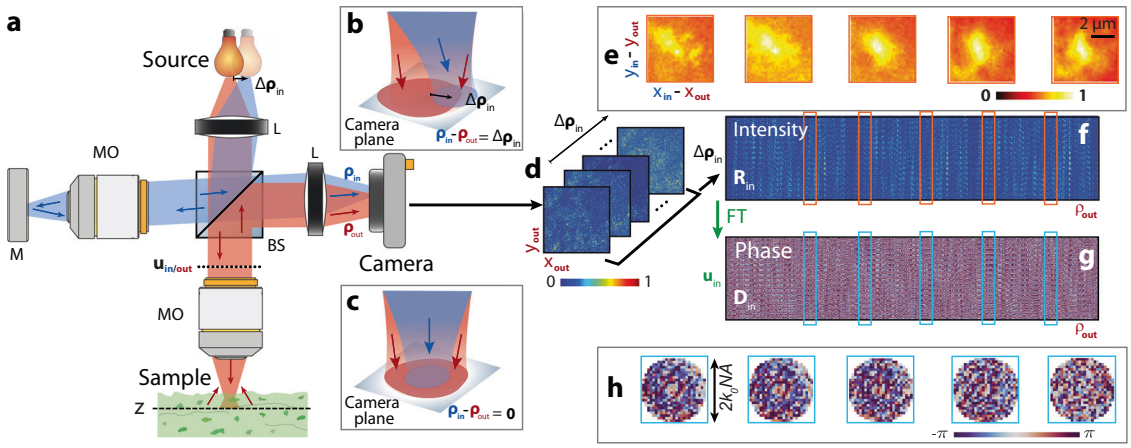

Fig. 1 | De-scanned measurement of the Reflection Matrix. a Experimental setup (L: lenses, MO: microscope objectives, M: reference mirror, BS: beam splitter). Light from an incoherent source is split into two replica laterally shifted with respect to each other by a relative position $\Delta\boldsymbol{\rho}$ (see Supplementary Section 1). By a game of polarization, each replica illuminates one arm of a Linnik interferometer. The sample beam (in red) illuminates the scattering sample through a microscope objective (NA = 1.0). The reference beam (in blue) is focused on a dielectric mirror through an identical microscope objective. Both reflected beams interfere on a CMOS camera whose surface is conjugated with focal planes of the MO. The amplitude and phase of the interference term are retrieved by phase-shifting interferometry. **b** Each pixel of the camera, depicted by its position $\boldsymbol{\rho}_{\text{out}}$, measures the reflection coefficient $R(\boldsymbol{\rho}_{\text{in}}, \boldsymbol{\rho}_{\text{out}}, z)$ between de-scanned focusing points, $\boldsymbol{\rho}_{\text{out}}$ and $\boldsymbol{\rho}_{\text{in}} = \boldsymbol{\rho}_{\text{out}} + \Delta\boldsymbol{\rho}_{\text{in}}$, at depth z within the sample. **c** For $\Delta\boldsymbol{\rho}_{\text{in}} = \mathbf{0}$, the experimental set up is equivalent to a FFOCT apparatus and the interferogram directly provides a time-gated confocal image of the sample. **d** The set of interferograms are stored in the de-scanned reflection matrix $\mathbf{R}_{\text{in}}(z) = [R_{\text{in}}(\Delta\boldsymbol{\rho}_{\text{in}}, \boldsymbol{\rho}_{\text{out}}, z)]$ displayed in (**f**). **e** Each column of this matrix yields a reflection point-spread function (RPSF) associated with the focusing quality at point $\boldsymbol{\rho}_{\text{out}}$ (scale bar: 2 μm). **g** The Fourier transform (FT) of each de-scanned wave-field provides the input distortion matrix $\mathbf{D}_{\text{in}}(z) = [D_{\text{in}}(\mathbf{u}_{\text{in}}, \boldsymbol{\rho}_{\text{out}}, z)]$. **h** Each column of this matrix displays the distorted wavefront associated with each point $\boldsymbol{\rho}_{\text{out}}$ in the field-of-view. The optical data shown in panels (**d**–**h**) correspond to the acquisition performed at depth z = 150 μm.

https://doi.org/10.1038/s41467-024-51619-9

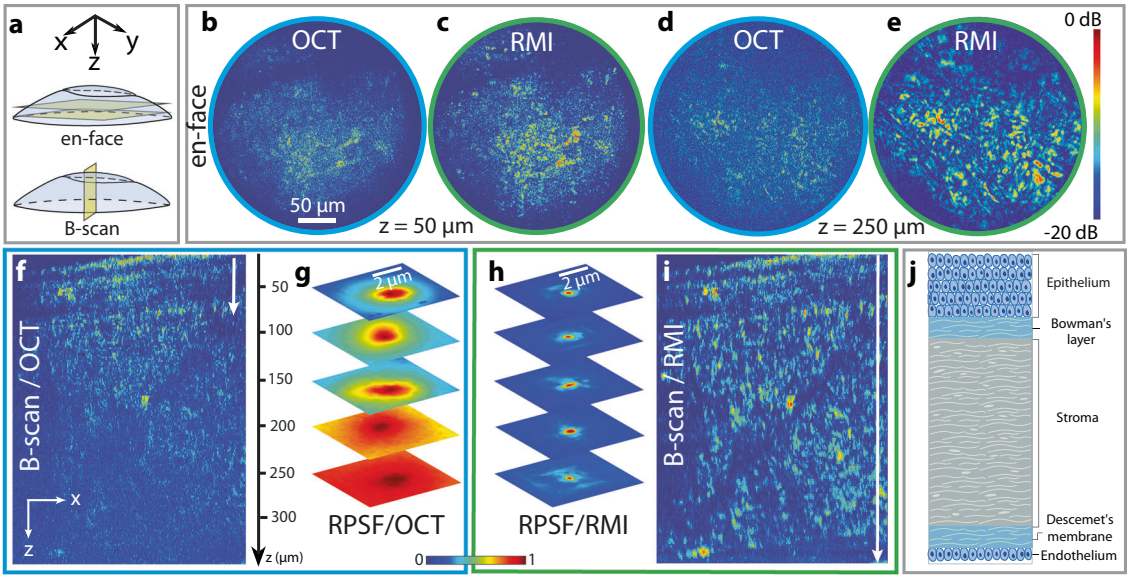

Fig. 2 | Volumetric matrix imaging of an opaque cornea. a Schematic of the imaging planes in the cornea. **b**, **c** *En-face* confocal images before (**b**) and after (**c**) the matrix imaging process for $z = 50\ \mu$m (scale bar: 50 μm). **d**, **e** *En-face* confocal images before (**d**) and after (**e**) the matrix imaging process for $z = 250\ \mu$m (scale bar: 50 μm). **f** Longitudinal (x,z) section of the initial confocal image. **g**, **h** Original (**g**) and corrected (**h**) RPSFs from $z = 50$ to 250 μm (scale bar: 2 μm). **i** Longitudinal (x,z) section of the volumetric image at the end of the matrix imaging process. **j** Schematic of a healthy human cornea. Each image is normalized at each depth by its averaged intensity.

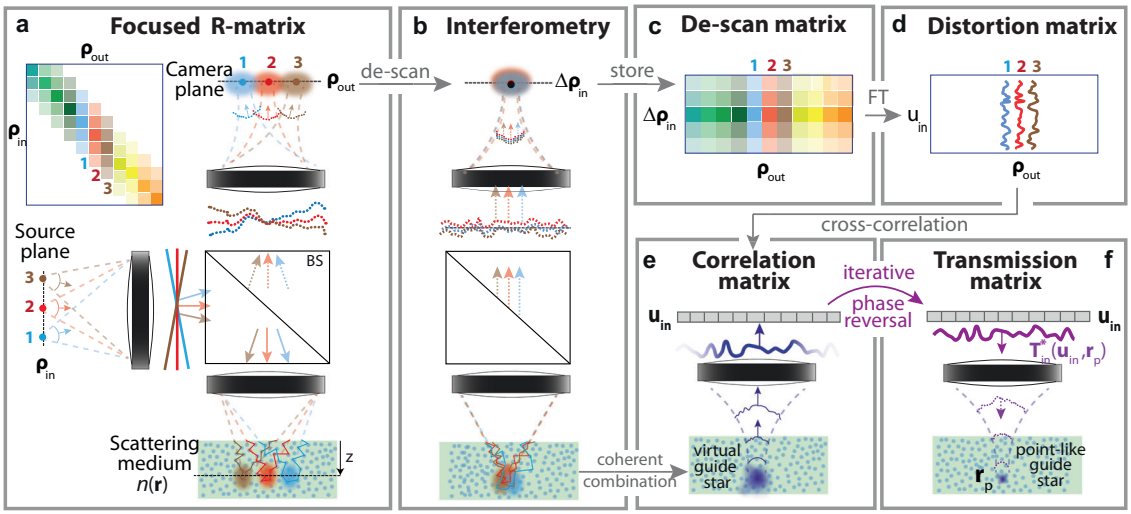

Fig. 3 | Different Stages of Matrix Imaging. a The focused **R**-matrix contains the set of impulse responses $R(\boldsymbol{\rho}_{in}, \boldsymbol{\rho}_{out}, z)$ between an array of point sources $\boldsymbol{\rho}_{in}$ and detectors $\boldsymbol{\rho}_{out}$ lying in planes conjugated with the focal plane of the microscope objective (BS: beam splitter). **b** The interferometric set up displayed in Fig. 1 allows a de-scanned measurement of **R** by scanning the relative position $\Delta\boldsymbol{\rho}_{in} = \boldsymbol{\rho}_{in} - \boldsymbol{\rho}_{out}$. **c** Each column of the recorded matrix $\mathbf{R}_{in}$(Eq. (1)) corresponds to the RPSF measured by each camera pixel. **d** A spatial Fourier transform (FT) over $\Delta\boldsymbol{\rho}_{in}$ provides the distortion matrix $\mathbf{D}_{in}$ (Eq. (5)) linking each camera pixel with wave-front distortions seen from the input pupil plane ($\mathbf{u}_{in}$). **e** The correlation matrix $\mathbf{C}_{in}$ between those wave-fronts mimics the time-reversal operator associated with a virtual guide star that results from a coherent average of all the de-scanned focal spots displayed in **b** (Supplementary Section 2). **f** IPR is then applied (Methods). The resulting wave-front compensates for aberrations and scattering inside the medium to produce a sharper guide star. It provides an estimation of one column of $\mathbf{T}_{in}$ corresponding to the common mid-point $\mathbf{r}_p$ of the input focal spots considered in (**a**).

recorded in parallel by the pixels of the camera in the imaging plane. Their amplitude and phase are retrieved by phase-stepping interferometry[28]. The FFOCT signal is thus equivalent to a time-gated confocal image of the sample[29]. Figure 2b, d and f show en-face and axial FFOCT images of the opaque cornea at different depths. A dramatic loss in contrast is found beyond the epithelium ($z > 70\ \mu$m, see Fig. 2j). It highlights the detrimental effect of multiple scattering for deep optical imaging.

To overcome the multiple scattering phenomenon, one should go beyond a simple confocal image and record the cross-talk between the camera pixels. Experimentally, it consists in measuring the reflection matrix **R** associated with the sample (Fig. 3a). Interestingly, this can be done by slightly modifying the illumination scheme of the FFOCT device, as displayed in Fig. 1a. The incident wave-fields are still identical in each arm but are laterally shifted with respect to each other by a transverse position $\Delta\boldsymbol{\rho}_{in}$. Their spatial incoherence now acts as a

de-scanned pinhole that gives access to the cross-talk between distinct focusing points (Fig. 1b). The interferogram recorded by the camera (Fig. 1d) directly provides one line of the reflection matrix $\mathbf{R}_{\text{in}}$ de-scanned at input (Fig. 3b,c), such that

$$R_{\text{in}}(\Delta\boldsymbol{\rho}_{\text{in}},\boldsymbol{\rho}_{\text{out}},z) = R(\boldsymbol{\rho}_{\text{out}} + \Delta\boldsymbol{\rho}_{\text{in}},\boldsymbol{\rho}_{\text{out}},z), \tag{1}$$

with $\mathbf{R} = [R(\boldsymbol{\rho}_{\text{in}}, \boldsymbol{\rho}_{\text{out}}, z)]$, the reflection matrix expressed in the canonical basis. Its coefficients $R(\boldsymbol{\rho}_{\text{in}}, \boldsymbol{\rho}_{\text{out}}, z)$ correspond to the response of the medium at depth z between points $\boldsymbol{\rho}_{\text{in}}$ and $\boldsymbol{\rho}_{\text{out}}$ in the source and camera planes (Fig. 3a). Scanning the relative position $\Delta\boldsymbol{\rho}_{\text{in}}$ is equivalent to recording the canonical $\mathbf{R}$-matrix diagonal-by-diagonal (see Fig. 3a,c). However, while a raster scan (column-by-column acquisition) of $\mathbf{R}$ requires to illuminate the sample over a field-of-view Ω with $N = (\Omega/\delta_0)^2$ input wave-fronts[20,31,32], the de-scanned basis allows a much smaller number of field measurements.

This sparsity can be understood by expressing theoretically the de-scan matrix $\mathbf{R}_{\text{in}}$ (Supplementary Section 2):

$$R_{\text{in}}(\Delta\boldsymbol{\rho}_{\text{in}},\boldsymbol{\rho}_{\text{out}},z) = \int_{\Omega} d\boldsymbol{\rho}_s\, H_{\text{in}}(\boldsymbol{\rho}_s + \Delta\boldsymbol{\rho}_{\text{in}},\boldsymbol{\rho}_{\text{in}},z)\gamma(\boldsymbol{\rho}_s + \boldsymbol{\rho}_{\text{out}},z)H_{\text{out}}(\boldsymbol{\rho}_s,\boldsymbol{\rho}_{\text{out}},z) \tag{2}$$

where γ is the sample reflectivity. $H_{\text{in}}(\boldsymbol{\rho}_s, \boldsymbol{\rho}_{\text{in}}, z)$ and $H_{\text{out}}(\boldsymbol{\rho}_s, \boldsymbol{\rho}_{\text{out}}, z)$ are the local input and output point spread functions (PSFs) at points $(\boldsymbol{\rho}_{\text{in}}, z)$ and $(\boldsymbol{\rho}_{\text{out}}, z)$, respectively. This last equation confirms that the central line of $\mathbf{R}_{\text{in}}$ ($\Delta\boldsymbol{\rho}_{\text{in}} = \mathbf{0}$), i.e. the FFOCT image, results from a convolution between the sample reflectivity γ and the local confocal PSF, $H_{\text{in}} \times H_{\text{out}}$.

The de-scanned elements allow us to go far beyond standard confocal imaging. In particular, they will be exploited to unscramble the local input and output PSFs in the vicinity of each focal point. As a preliminary step, they can also be used to quantify the level of aberrations and multiple scattering. In average, the de-scanned intensity, $I(\Delta\boldsymbol{\rho}_{\text{in}}, \boldsymbol{\rho}_{\text{out}}, z) = |R_{\text{in}}(\Delta\boldsymbol{\rho}, \boldsymbol{\rho}_{\text{out}}, z)|^2$, can actually be expressed as the convolution between the incoherent input and output PSFs[33]:

$$\langle I(\Delta\boldsymbol{\rho}_{\text{in}},\boldsymbol{\rho}_{\text{out}},z)\rangle \propto |H_{\text{in}}|^2 \overset{\Delta\boldsymbol{\rho}_{\text{in}}}{\circledast} |H_{\text{out}}|^2(\Delta\boldsymbol{\rho}_{\text{in}},\boldsymbol{\rho}_{\text{out}},z) \tag{3}$$

where the symbol $\circledast$ stands for convolution product and $\langle \cdots \rangle$ for ensemble average. This quantity will be referred to as RPSF in the following (acronym for reflection PSF). Figure 1e displays examples of RSPF extracted in depth of the opaque cornea. The spatial extension δ_R of the RPSF indicates the focusing quality and dictates the number M of central lines of $\mathbf{R}_{\text{in}}(z)$ that contain the relevant information for imaging:

$$M \sim (\delta_R/\delta_0)^2 \tag{4}$$

with $\delta_0 \sim \lambda/(4NA)$, the confocal maximal resolution of the imaging system. For a field-of-view much larger than the spatial extension of the RPSF ($\Omega \gg \delta_R$), the de-scanned basis is thus particularly relevant for the acquisition of $\mathbf{R}$ ($M \ll N$).

Quantifying the focusing quality

Figure 2 g shows the depth evolution of the RPSF. It exhibits the following characteristic shape: a distorted and enlarged confocal spot due to aberrations on top of a diffuse background[33]. While the latter component is due to multiple scattering, the former component contains the contribution of singly-scattered photons but also a coherent backscattering peak[33] resulting from a constructive interference between multiple scattering paths[34,35] (Supplementary Fig. 13).

Figure 2 g clearly highlights two regimes. In the epithelium ($z < 70\ \mu$m), the single scattering component is predominant and the image of the cornea is reliable although its resolution is affected by aberrations (Fig. 2b). Beyond this depth, the multiple scattering background is predominant and drastically blurs the image (Fig. 2d). The axial evolution of the single scattering rate enables the measurement of the scattering mean free path ℓ_s[36] (Supplementary Section 4). We find $\ell_s \sim 35\ \mu$m in the stroma (Fig. 2j), which confirms the strong opacity of the cornea. The penetration depth limit thus scales as $2\ell_s$. This value is modest compared with theoretical predictions[8] ($\sim 4\ell_s$) but is explained by the occurrence of strong aberrations at shallow depths, partially due to the index mismatch at the cornea surface (Fig. 2g).

The RSPF also fluctuates in the transverse direction. To highlight this variation, a map of local RPSFs (Fig. 4b) can be built by considering the back-scattered intensity over limited spatial windows (Methods). This map shows important fluctuations due to: (i) the variations of the medium reflectivity that acts on the level of the confocal spot with respect to the diffuse background; (ii) the lateral variations of the optical index upstream of the focal plane that induce distortions of the confocal peak. Such complexity implies that any point in the medium will be associated with its own distinct focusing law. Nevertheless, spatial correlations subsist between RSPFs in adjacent windows (Fig. 4b). Such correlations can be explained by a physical phenomenon often referred to as isoplanatism in AO[37] and that results in a locally-invariant PSF[38]. We will now see how this local isoplanicity can be exploited for the estimation of the $\mathbf{T}$-matrices.

Iterative phase reversal of wave distortions

To that aim, we will exploit and extend the distortion matrix concept introduced in a previous work[19]. Interestingly, a Fourier transform over the coordinate $\Delta\boldsymbol{\rho}_{\text{in}}$ of each de-scanned wave-field, $R_{\text{in}}(\Delta\boldsymbol{\rho}_{\text{in}}, \boldsymbol{\rho}_{\text{out}}, z)$, actually yields the wave distortions seen from the input pupil plane (Fig. 3d) :

$$\mathbf{D}_{\text{in}}(z) = \mathbf{T}_0 \times \mathbf{R}_{\text{in}}(z) \tag{5}$$

where $\mathbf{T}_0$ denotes the Fourier transform operator, $T_0(\mathbf{u},\Delta\boldsymbol{\rho}) = \exp(-i2\pi\mathbf{u}.\Delta\boldsymbol{\rho}/\lambda f)$, λ the central wavelength and f the MO focal length. $\mathbf{D}_{\text{in}}(z) = [D(\mathbf{u}_{\text{in}}, \boldsymbol{\rho}_{\text{out}}, z)]$ is the distortion matrix that connects any voxel $(\boldsymbol{\rho}_{\text{out}}, z)$ in the field-of-view to wave-distortions in the input pupil plane $(\mathbf{u}_{\text{in}})$.

As expected in most of biological tissues, this matrix exhibits local correlations that can be understood in light of the shift-shift memory effect[38,39]: Waves produced by nearby points inside an anisotropic scattering medium generate highly correlated random speckle patterns in the pupil plane. Figure 1 illustrates this fact by displaying an example of distortion matrix (Fig. 1g) and reshaped distorted wavefields for different points $(\boldsymbol{\rho}_{\text{out}}, z)$ (Fig. 1h). A strong similarity can be observed between distorted wave-fronts associated with neighboring points but this correlation tends to vanish when the two points are too far away.

The next step is to extract and exploit this local memory effect for imaging. To that aim, a set of correlation matrices $\mathbf{C}_{\text{in}}(\mathbf{r}_{\text{p}})$ shall be considered between distorted wave-fronts in the vicinity of each point $\mathbf{r}_{\text{p}}$ in the field-of-view (Methods). Under the hypothesis of local isoplanicity, each matrix $\mathbf{C}_{\text{in}}(\mathbf{r}_{\text{p}})$ is analogous to a $\mathbf{R}$-matrix associated with a virtual reflector synthesized from the set of output focal spots[21] (see Fig. 3e and Supplementary Section 2). In this fictitious experimental configuration, an iterative phase-reversal (IPR) process can be performed to converge towards the incident wave front that focuses perfectly through the heterogeneities of the medium onto this virtual guide star (see Fig. 3f and Methods).

IPR repeated for each point $\mathbf{r}_{\text{p}}$ yields a set of pupil phase laws $\mathcal{T}_{\text{in}}(\mathbf{u},\mathbf{r}_p)$ forming the transmittance matrix $\boldsymbol{\mathcal{T}}_{\text{in}}$. Its digital phase conjugation enables a local compensation of aberration and forward multiple scattering. An updated de-scanned matrix can then be built:

$$\mathbf{R}_{\text{in}} = \mathbf{T}_0^{\dagger} \times \left[\boldsymbol{\mathcal{T}}^{*}_{\text{in}} \circ \mathbf{D}_{\text{in}}\right] \tag{6}$$

https://doi.org/10.1038/s41467-024-51619-9

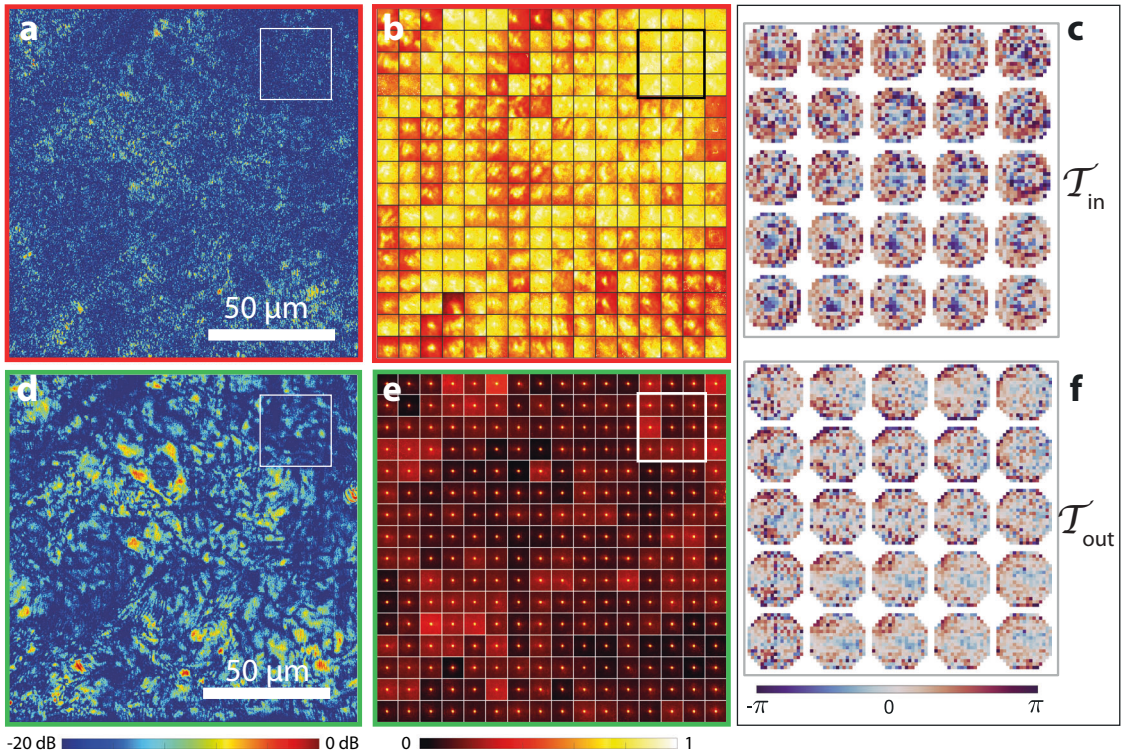

Fig. 4 | Time-gated Transmission Matrix for Local Compensation of Forward Multiple Scattering. a Raw confocal image of the cornea at 200 μm-depth (scale bar: 50 μm). **b** Map of the local reflection point-spread functions (RPSFs) (de-scan: 7×7 μm^2) over the field of view. **c** Sub-part of transmittance matrix $\mathcal{T}_{in}$ for the area delimited by the square box in (**a**). **d** Matrix image at 200 μm-depth after the multi-scale compensation of aberrations and forward multiple scattering (scale bar: 50 μm). **e** Map of the local RPSFs after the matrix imaging process (de-scan: 7×7 μm^2) over the field of view. **f** Sub-part of transmittance matrix $\mathcal{T}_{out}$ for the area delimited by the square box in (**a**).

where the symbol † stands for transpose conjugate and ∘ for the Hadamard product. The same process can be repeated by exchanging input and output to estimate the output transmittance matrix $\mathcal{T}_{out}$ (Methods). The element wise product between the free space transmission matrix $\mathbf{T}_0$ and the transmittance matrix $\mathcal{T}$ constitutes an estimator of the time-gated transmission matrix $\mathbf{T}$. The latter matrix contains the impulse responses $T(\mathbf{u}, \mathbf{r})$ between the pupil plane $\mathbf{u}$ and each voxel $\mathbf{r}$ inside the medium around the ballistic time τ_B. Note that this matrix not only contains a ballistic (possibly aberrated) component but also grasps forward multiple scattering paths which display a time-of-flight in the same coherence time as ballistic photons. In the following, we show how these complex trajectories can be harnessed thanks to RMI.

Multi-scale analysis of the distortion matrix

To that aim, a critical aspect is the choice of the spatial window over which wave distortions shall be analyzed. On the one hand, the isoplanatic assumption is valid for low-order aberrations that are associated with extended isoplanatic patches. On the other hand, forward multiple scattering gives rise to high-order aberrations that exhibit a coherence length that decreases with depth until reaching the size of a speckle grain beyond ℓ_t[38]. However, each spatial window should be large enough to encompass a sufficient number of independent realizations of disorder[40]. Indeed, the bias of our $\mathbf{T}$ − matrix estimator scales as follows (see Supplementary Section 3):

$$|\delta\mathcal{T}(\mathbf{u},\mathbf{r}_p)|^2 \sim 1/(\mathcal{C}^2 N_W) \quad (7)$$

with N_W the number of resolution cells in each spatial window. C is a coherence factor that is a direct indicator of the focusing quality[41].

To limit this bias while addressing the scattering component of $\mathcal{T}$, an iterative multi-scale analysis of $\mathbf{D}$ is proposed (Methods). It consists in gradually reducing the size of the virtual guide star by: (*i*) alternating the correction at input and output (Supplementary Section 3); (*ii*) dividing by two the size of overlapping spatial windows at each iterative step (Fig. 5a). Thereby the RPSF extension is gradually narrowed (Fig. 5b) and the coherence factor $\mathcal{C}$ increased. The spatial window can thus be reduced accordingly at the next step while maintaining an acceptable bias (Eq. (7)). It enables the capture of finer angular and spatial details of the $\mathcal{T}-$ matrix at each step (Fig. 5c) while ensuring the convergence of IPR. As discussed further, the end of the process is monitored by the memory effect that shall exhibit the $\mathcal{T}-$ matrix (Supplementary Section 3). The whole process is validated by a reference imaging experiment on a resolution target placed behind an opaque tissue layer (Supplementary Fig. 8).

Transmittance matrix and memory effect

Figure 4 c and f show a sub-part of the $\mathcal{T}-$ matrices measured at depth $z = 200$ μm for final patches of 6×6 μm^2. Spatial reciprocity should imply equivalent input and output aberration phase laws. This property is not checked by our estimators. Indeed, the input aberration phase law accumulates not only the input aberrations of the sample-arm but also those of the reference arm (Supplementary Section 4). Therefore, the sample-induced aberrations can be investigated independently from the imperfections of the experimental set up by considering the output matrix $\mathcal{T}_{out}$.

An analysis of its spatial correlations[40] (Methods) and its angular decomposition (Supplementary Fig. 12) shows that wave distortions induced by the cornea are made of two contributions: (i) an almost spatially-invariant aberrated component (Fig. 6a) associated with long-

https://doi.org/10.1038/s41467-024-51619-9

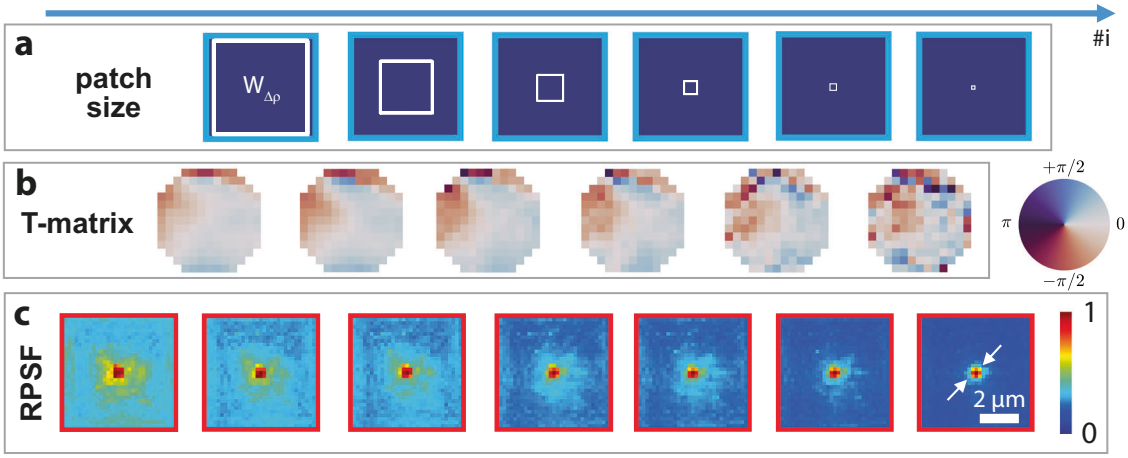

Fig. 5 | Multi-scale analysis of wave distortions. a The entire field-of-view is 138 × 138 μm^2. At each step, it is divided into a set of spatial windows whose dimension gradually decreases: from 138, 100, 50, 25, 13 to 6 μm. **b** Evolution of the pupil transmittance $\mathcal{T}(\mathbf{u}_{out},\mathbf{r}_p)$ for one point $\mathbf{r}_p$ of the field-of-view at each iteration step. **c** Corresponding local RPSF at $\mathbf{r}_p$ before and after compensation of aberration and scattering using digital phase-conjugation of the optical transfer function displayed in (**b**) (scale bar: 2 μm). Data are from the cross-section at 200 μm depth within the sample.

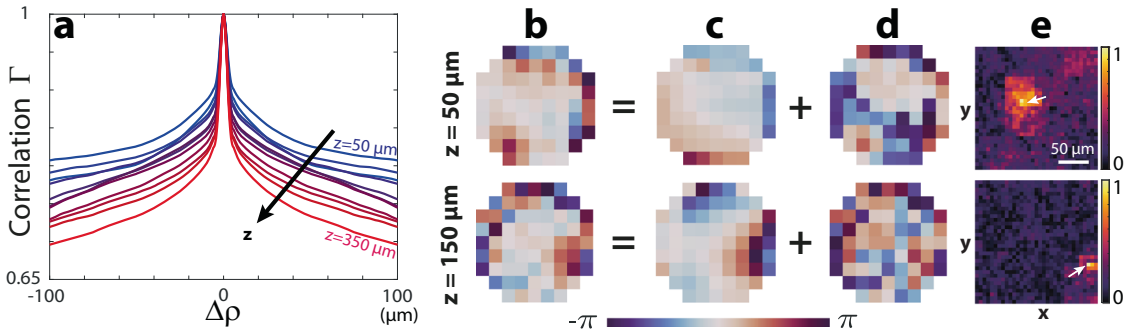

Fig. 6 | Revealing the memory effect exhibited by the $\mathcal{T}-$ matrix. a Transverse evolution of the mean correlation function of the transmitted wave-field from shallow (blue) to large (red) depths. **b** The phase of each transmitted wave-field is the sum of: **c** a spatially-invariant aberration phase function; **d** a complex scattering law exhibiting high spatial frequencies. **e** The spatial correlation of the latter component with the $\mathcal{T}-$ matrix provides a map of the corresponding isoplanatic patch (scale bar: 50 μm).

scale fluctuations of the refractive index (Fig. 6c) ; (ii) a forward multiple scattering component (Fig. 6d) giving rise to an angular dispersion of photons between the cornea surface and the focal plane. The latter component is associated with a short-range memory effect whose extension drastically decreases in depth (Fig. 6a, e). The access to this contribution fundamentally differentiates RMI from conventional AO that only provides an access to the irrotational component of wave distortions[42] (Supplementary Section 4).

The memory effect is also a powerful tool to monitor the convergence of the IPR process. When the spatial window is too small (3 × 3 μm^2), IPR provides a spatially-incoherent $\mathcal{T}-$ matrix and leads to a bucket-like image (Supplementary Fig. 7). This observable thus indicates when the convergence towards $\mathcal{T}$ is fulfilled or when the algorithm shall be stopped.

Deep Volumetric Imaging

Eventually, the $\mathcal{T}$-matrix can be used to compensate for local aberrations over the whole field-of-view. To that aim, a digital phase conjugation is performed at input and output (Eq. (6)). The comparison between the initial and resulting images (Fig. 4a,d) demonstrates the benefit of a local compensation of aberration and scattering. The drastic gain in resolution and contrast provided by RMI enables to reveal a rich arrangement of biological structures (cells, striae, *etc.*) that were completely blurred by scattering in the initial image. For instance, a stromal stria, indicator of keratoconus[43], is clearly revealed on the RMI B-scan (Fig. 2i) while it was hidden by the multiple scattering fog on the initial image (Fig. 2f). The B-scan shows that RMI provides a full image of the cornea with the recovery of its different layers throughout its thickness (350 μm ~ $10\ell_s$, see also Supplementary Movies).

The gain in contrast and resolution can be quantified by investigating the RSPF after RMI. A close-to-ideal confocal resolution (230 nm vs. δ_0 ~ 215 nm) is reached throughout the cornea thickness (Fig. 2h). The confocal-to-diffuse ratio is increased by a factor up to 15 dB in depth (Supplementary Section 4). Furthermore, the map of local RPSFs displayed in Fig. 4e shows the efficiency of RMI for addressing extremely small isoplanatic patches.

Discussion

In this experimental proof-of-concept, we demonstrated the capacity of RMI to exploit forward multiple scattering for deep imaging of biological tissues. This work introduces several crucial elements, thereby leading to a better imaging performance than previous studies.

First, the proposed IPR algorithm outperforms iterative time reversal processing[19] for local compensation of aberrations in scattering media because it can evaluate the focusing laws over a larger

angular domain (Supplementary Fig. 2). Second, the bias of our **T**-matrix estimator has been expressed analytically (Eq. (7)) as a function of a coherence factor that grasps the blurring effect of aberrations and multiple scattering. This led us to define a multi-scale strategy for matrix imaging with a fine monitoring of its convergence based on the memory effect. The latter observable is a real asset as it provides an objective criterion to: (*i*) optimize the resolution of our **T** − matrix estimator (Supplementary Section 3); (*ii*) compare our approach with alternative methods such as the CLASS algorithm[20,23,24] (Supplementary Section 5). Our multi-scale process enables us to target isoplanatic areas more than four times smaller than CLASS. Interestingly, those two approaches are based on the maximization of different physical quantities: the confocal intensity for CLASS; the coherence of the wave-field induced by a virtual guide star for IPR. Hence they are, in principle, perfectly complementary and could be advantageously combined in the future.

Although this experimental proof-of-concept is promising for deep optical imaging of biological tissues, it also suffers from several limitations that need to be addressed in future works. First, FFOCT is not very convenient for 3D in-vivo imaging since it requires an axial scan of the sample. Another possibility would be to move the reference arm and measure **R** as a function of the time-of-flight. An access to the time (or spectral) dependence of the **R** − matrix is actually critical to reach a larger penetration depth. Indeed, the focusing law extracted from a time-gated **R** − matrix is equivalent in the time domain to a simple application of time delays between each angular component of the wave-field. Yet, the diffusive regime requires to address independently each frequency component of the wave-field to make multiple scattering paths of different lengths constructively interfere on any focusing point in depth. On the one hand, the exploitation of the chromato-axial memory effect[44] will be decisive to ensure the convergence of IPR over isoplanatic volumes[45]. On the other hand, the tilt-tilt memory effect[39] can also be leveraged by investigating the distortion matrix, not only in the pupil plane, but in any plane lying between the medium surface and the focal plane, thereby mimicking a multi-conjugate AO scheme[46].

Beyond the diffusive regime, another blind spot of this study is the medium movement during the experiment[47,48]. In that respect, the matrix formalism shall be developed to include the medium dynamics. Moving speckle can actually be an opportunity since it can give access to a large number of speckle realizations for each voxel. A high resolution **T** − matrix could be, in principle, extracted without relying on any isoplanatic assumption[49].

To conclude, this study is a striking illustration of a pluridisciplinary approach in wave physics. A passive measurement of the **R** − matrix is indeed an original idea coming from seismology[50]. The **D** − matrix is inspired by stellar speckle interferometry in astronomy[51]. The **T** − matrix is a concept that has emerged both from fundamental studies in condensed matter physics[52] and more applied fields such as MIMO communications[53] and ultrasound therapy[12]. The emergence of high-speed cameras and the rapid growth of computational capabilities now makes matrix imaging mature for deep in-vivo optical microscopy.

Methods

Experimental set up

The full experimental setup is displayed in Supplementary Fig. 1. It is made of two parts: (*i*) a polarized Michelson interferometer illuminated by a broadband LED source (Thorlabs M850LP1, λ_0 = 850 nm, $\Delta\lambda$ = 35 nm) in a pseudo-Kohler configuration, thereby providing at its output two identical spatially-incoherent and broadband wave-fields of orthogonal polarization, the reference one being shifted by a lateral position $\Delta\boldsymbol{\rho}_{\text{in}}$ by tilting the mirror in the corresponding arm; (*ii*) a polarized Linnik interferometer with microscope objectives (Nikon N60X-NIR, M = 60 × , NA = 1.0) in the two arms and a CMOS camera (Adimec Quartz 2A-750, 2Mpx) at its output. The de-scanned beam at the output the first interferometer illuminates the reference arm of the second interferometer and is reflected by the reference mirror placed in the focal plane of the MO. The other beam at the output of the first interferometer illuminates the sample placed in the focal plane of the other MO. The CMOS camera, conjugated with the focal planes of the MO, records the interferogram between the beams reflected by each arm of the Linnik interferometer. The spatial sampling of each recorded image is δ_0 = 230 nm and the field-of-view is 275 × 275 μm^2.

Cornea

The human cornea under study is a pathological surgical specimen that was provided by the Quinze-Vingts National Eye Hospital operating room at the time of keratoplasty. The use of such specimens was approved by the Institutional Review Board (Patient Protection Committee, Ile-de-France V) and adhered to the tenets of the Declaration of Helsinki as well as to international ethical requirements for human tissues. The ethics committee waived the requirement for informed written consent of patient; however, the patient provided informed oral consent to have their specimen used in research.

Experimental procedure

The experiment consists in the acquisition of the de-scanned reflection matrix $\mathbf{R}_{\text{in}}$. To that aim, an axial scan of the sample is performed over the cornea thickness (350 μm) with a sampling of 2 μm (i.e 185 axial positions). For each depth, a transverse scan of the de-scanned position $\Delta\boldsymbol{\rho}_{\text{in}}$ is performed over a 2.9 × 2.9 μm^2 area with a spatial sampling δ_0 = 230 nm (that is to say 169 input wave-fronts instead of 10^6 input wave-fronts in a canonical basis). For each scan position ($\Delta\boldsymbol{\rho}$, z), a complex-reflected wave field is extracted by phase shifting interferometry from four intensity measurements. This measured field is averaged over 5 successive realisations (for denoising). The integration time of the camera is set to 5 ms. Each wave-field is stored in the de-scanned reflection matrix $\mathbf{R}_{\text{in}} = [R_{\text{in}}(\Delta\boldsymbol{\rho}_{\text{in}}, \boldsymbol{\rho}_{\text{out}})]$ (Fig. 1). The duration time for the recording of $\mathbf{R}_{\text{in}}$ is of ~ 30 s at each depth. The post-processing of the reflection matrix (IPR and multi-scale analysis) to get the final image took only a few minutes on Matlab. The experimental results displayed in Figs. 4 and 5 at a single depth z = 200 μm have been obtained by performing a de-scan over a 7 × 7 μm^2 area with a spatial sampling δ_0 = 230 nm (961 input wave-fronts).

Local RPSF

To probe the local RPSF, the field-of-view is divided into regions that are defined by their central midpoint $\mathbf{r}_{\text{p}} = (\boldsymbol{\rho}_{\text{p}}, z)$ and their lateral extension L. A local average of the back-scattered intensity can then be performed in each region:

$$I(\Delta\boldsymbol{\rho}_{\text{in}}, \mathbf{r}_{\text{p}}) = \langle |R_{\text{in}}(\Delta\boldsymbol{\rho}_{\text{in}}, \boldsymbol{\rho}_{\text{out}}, z)|^2 W_L(\boldsymbol{\rho}_{\text{out}} - \boldsymbol{\rho}_{\text{p}}) \rangle_{\boldsymbol{\rho}_{\text{out}}} \tag{8}$$

where $W_L(\boldsymbol{\rho}_{\text{out}} - \boldsymbol{\rho}_{\text{p}}) = 1$ for $|x_{\text{out}} - x_{\text{p}}| < L$ and $|y_{\text{out}} - y_{\text{p}}| < L$, and zero otherwise.

Multi-scale compensation of wave-distortions

The multi-scale process consists in an iterative compensation of aberration and scattering phenomena at input and output of the reflection matrix. To that aim, wave distortions are analyzed over spatial windows W_L that are gradually reduced at each step q of the procedure, such that:

$$L = FOV/2^q \tag{9}$$

where *FOV* denotes the initial field-of-view.

The whole procedure is summarized in Supplementary Fig. 4. At each stage of this iterative process, the starting point is the de-scanned reflection matrix $\mathbf{R}_{\text{in}}^{(q-1)}$, obtained at the previous step, $\mathbf{R}_{\text{in}}^{(0)}$ being the reflection matrix recorded by our experimental set up (Fig. 1). An input distortion matrix $\mathbf{D}_{\text{in}}^{(q)}$ is deduced from $\mathbf{R}_{\text{in}}^{(q)}$ via a numerical Fourier

transform (Eq. (5)). A local correlation matrix of wave distortions is then built around each point $\mathbf{r}_p$ of the field-of-view:

$$C_{in}(\mathbf{u}_{in},\mathbf{u}'_{in},\mathbf{r}_p)=\left\langle D_{in}^{(q)}(\mathbf{u}_{in},\boldsymbol{\rho}_{out},z)D_{in}^{(q)*}(\mathbf{u}'_{in},\boldsymbol{\rho}_{out},z)W_L(\boldsymbol{\rho}_{out}-\boldsymbol{\rho}_p)\right\rangle_{\boldsymbol{\rho}_{out}} \tag{10}$$

IPR is then applied to each correlation matrix $\mathbf{C}_{in}(\mathbf{r}_p)$ (see further and Supplementary Section 3). The resulting input phase laws, $\hat{\boldsymbol{\phi}}_{in}(\mathbf{r}_p)$, are used to compensate for the wave distortions undergone by the incident wave-fronts:

$$\mathbf{R}'_{in}=\mathbf{T}_0^{\dagger}\times\left[\exp\left(-i\hat{\boldsymbol{\phi}}_{in}\right)\circ\mathbf{D}_{in}^{(q-1)}\right] \tag{11}$$

The corrected matrix $\mathbf{R}'_{in}$ is only intermediate since phase distortions undergone by the reflected wave-fronts remain to be corrected.

To that aim, an output de-scanned matrix $\mathbf{R}'_{out}(z)$ is deduced from the input de-scanned matrix $\mathbf{R}'_{in}(z)$ using the following change of variable (Supplementary Fig. 5):

$$R'_{out}(\boldsymbol{\rho}_{in},\Delta\boldsymbol{\rho}_{out},z)=R'_{in}(-\Delta\boldsymbol{\rho}_{out},\boldsymbol{\rho}_{in}+\Delta\boldsymbol{\rho}_{out},z) \tag{12}$$

with $\Delta\boldsymbol{\rho}_{out}=\boldsymbol{\rho}_{out}-\boldsymbol{\rho}_{in}=-\Delta\boldsymbol{\rho}_{in}$. An output distortion matrix is then built by applying a Fourier transform over the de-scanned coordinate:

$$\mathbf{D}'_{out}=\mathbf{R}'_{out}\times\mathbf{T}_0^{T} \tag{13}$$

where the superscript ^{T} stands for matrix transpose. From $\mathbf{D}'_{out}$, one can build a correlation matrix $\mathbf{C}_{out}$ for each point $\mathbf{r}_p$:

$$C_{out}(\mathbf{u}_{out},\mathbf{u}'_{out},\mathbf{r}_p)=\left\langle D'_{out}(\boldsymbol{\rho}_{in},\mathbf{u}_{out},z_p)D'^{*}_{out}(\boldsymbol{\rho}_{in},\mathbf{u}'_{out},z_p)W_L(\boldsymbol{\rho}_{in}-\boldsymbol{\rho}_p)\right\rangle_{\boldsymbol{\rho}_{in}} \tag{14}$$

The IPR algorithm described further is then applied to each matrix $\mathbf{C}_{out}(\mathbf{r}_p)$. The resulting output phase laws, $\hat{\boldsymbol{\phi}}_{out}(\mathbf{r}_p)$, are leveraged to compensate for the residual wave distortions undergone by the reflected wave-fronts:

$$\mathbf{R}_{out}^{(q)}=\left[\mathbf{D}'_{out}\circ\exp\left(-i\boldsymbol{\phi}_{out}\right)\right]\times\mathbf{T}_0^{*} \tag{15}$$

The RPSFs displayed in Fig. 5c are extracted from the matrices $\mathbf{R}_{out}^{(q)}$ obtained at the end of each iteration of the multi-scale process. An input de-scanned matrix, combining the input and output corrections, is finally obtained by performing the following change of variables:

$$R_{in}^{(q)}(\Delta\boldsymbol{\rho}_{in},\boldsymbol{\rho}_{out},z)=R_{out}^{(q)}(\boldsymbol{\rho}_{out}-\Delta\boldsymbol{\rho}_{in},-\Delta\boldsymbol{\rho}_{in},z) \tag{16}$$

This matrix $\mathbf{R}_{in}^{(q)}$ is the starting point of the next stage of the multi-scale process, and so on.

The $\mathcal{T}$-matrices correspond to the cumulative function of the aberration phase laws:

$$\mathcal{T}_{in/out}^{(q)}=\mathcal{T}_{in/out}^{(q-1)}\circ\exp\left(i\boldsymbol{\phi}_{in/out}^{(q)}\right)=\prod_{k=1}^{q}\exp\left(i\boldsymbol{\phi}_{in/out}^{(k)}\right) \tag{17}$$

Figure 5b shows the evolution of one line of the transmittance matrix $\mathcal{T}_{out}^{(q)}$ throughout the RMI process. The iterative procedure is stopped by investigating the correlation properties of this estimator (see further and Supplementary Section 3).

Iterative phase reversal algorithm

The IPR algorithm is a computational process that provides an estimator of the pupil transmittance matrix, $\mathcal{T}(\mathbf{u},\mathbf{r}_p)=\exp\left[i\boldsymbol{\phi}(\mathbf{u},\mathbf{r}_p)\right]$, that links each point $\mathbf{u}$ of the pupil plane with each voxel $\mathbf{r}_p$ of the cornea volume. To that aim, the correlation matrix $\mathbf{C}$ computed over the spatial window W_L centered around each point $\mathbf{r}_p$ is considered (Eqs. (10) and (14)). Mathematically, the algorithm is based on the following recursive relation:

$$\hat{\boldsymbol{\phi}}^{(n)}(\mathbf{r}_p)=\arg\left\{\mathbf{C}(\mathbf{r}_p)\times\exp\left[i\hat{\boldsymbol{\phi}}^{(n-1)}(\mathbf{r}_p)\right]\right\} \tag{18}$$

where $\hat{\boldsymbol{\phi}}^{(n)}$ is the estimator of $\boldsymbol{\phi}$ at the n^{th} iteration of the phase reversal process. $\hat{\boldsymbol{\phi}}^{(0)}$ is an arbitrary wave-front that initiates the process (typically a flat phase law) and $\hat{\boldsymbol{\phi}}=\lim_{n\to\infty}\hat{\boldsymbol{\phi}}^{(n)}$ is the result of IPR.

Aberration and scattering components of the T-matrix

The spatial correlation of transmitted wave-fields are investigated at each depth z by computing the correlation matrix of $\mathcal{T}_{out}$: $\mathbf{C}_{\mathcal{T}}=\mathcal{T}_{out}\times\mathcal{T}_{out}^{\dagger}$. A mean correlation function Γ can be computed by performing the following average:

$$\Gamma(\Delta\boldsymbol{\rho},z)=\left\langle C_{\mathcal{T}}(\boldsymbol{\rho}_{in},\boldsymbol{\rho}_{in}+\Delta\boldsymbol{\rho},z)\right\rangle_{\boldsymbol{\rho}_{in}} \tag{19}$$

The correlation function Γ displayed in Fig. 6a shows that the matrix $\mathcal{T}_{out}$ can be decomposed as a spatially-invariant component $\mathcal{A}_{out}$ and a short-range correlated component $\mathcal{S}_{out}$. Each component can be separated by performing a singular value decomposition of $\mathcal{T}_{out}$, such that

$$\mathcal{T}_{out}=\sum_{p=1}^{N}s_p\mathbf{U}_p\mathbf{V}_p^{\dagger} \tag{20}$$

where s_p are the positive and real singular values of $\mathcal{T}_{out}$ sorted in decreasing order, $\mathbf{U}_p$ and $\mathbf{V}_p$ are unitary matrices whose columns correspond to the singular vectors of $\mathcal{T}_{out}$ in the pupil and focal planes, respectively. The first eigenspace of $\mathcal{T}_{out}$ provides its spatially-invariant aberrated component: $\mathcal{A}_{out}=s_1\mathbf{U}_1\mathbf{V}_1^{\dagger}$. The higher rank eigenstates provide the forward multiple scattering component $\mathcal{S}_{out}$. Lines or columns of the associated correlation matrix $\mathbf{C}_{\mathcal{S}}=\mathcal{S}_{out}\times\mathcal{S}_{out}^{\dagger}$ provides the isoplanatic patches displayed in Fig. 6e.

Reporting summary

Further information on research design is available in the Nature Portfolio Reporting Summary linked to this article.

Data availability

The optical data generated in this study are available at Zenodo[54] (https://zenodo.org/record/7665117).

Code availability

Codes used to post-process the optical data within this paper are available from the corresponding author.

References

1. Gérardin, B., Laurent, J., Derode, A., Prada, C. & Aubry, A. Full transmission and reflection of waves propagating through a maze of disorder. *Phys. Rev. Lett.* **113**, 173901 (2014).
2. Horodynski, M., Kühmayer, M., Ferise, C., Rotter, S. & Davy, M. Anti-reflection structure for perfect transmission through complex media. *Nature* **607**, 281 (2022).
3. Billy, J. et al. Direct observation of anderson localization of matter waves in a controlled disorder. *Nature* **453**, 891 (2008).
4. Hu, H., Strybulevych, A., Page, J. H., Skipetrov, S. E. & van Tiggelen, B. A. Localization of ultrasound in a three-dimensional elastic network. *Nat. Phys.* **4**, 945 (2008).
5. Ntziachristos, V. Going deeper than microscopy: The optical imaging frontier in biology. *Nat. Methods* **7**, 603 (2010).
6. Bertolotti, J. & Katz, O. Imaging in complex media. *Nat. Phys.* **18**, 1008 (2022).

7. Dunsby, C. & French, P. Techniques for depth-resolved imaging through turbid media including coherence-gated imaging. *J. Phys. D: Appl. Phys.* **36**, R207 (2003).
8. Badon, A., Boccara, A. C., Lerosey, G., Fink, M. & Aubry, A. Multiple scattering limit in optical microscopy. *Opt. Express* **25**, 28914 (2017).
9. Huang, D. et al. Optical coherence tomography. *Science* **254**, 1178 (1991).
10. Babcock, H. W. The possibility of compensating astronomical seeing. *Publ. Astronomical Soc. Pacific* **65**, 229 (1953).
11. Booth, M. J. Adaptive optical microscopy: The ongoing quest for a perfect image. *Light Sci Appl* **3**, e165 (2014).
12. Tanter, M., Aubry, J.-F., Gerber, J., Thomas, J.-L. & Fink, M. Optimal focusing by spatio-temporal inverse filter. I. Basic principles. *J. Acoust. Soc. Am.* **110**, 37 (2001).
13. Derode, A. et al. Taking advantage of multiple scattering to communicate with time-reversal antennas. *Phys. Rev. Lett.* **90**, 014301 (2003).
14. Popoff, S. M. et al. Measuring the transmission matrix in optics: An approach to the study and control of light propagation in disordered media. *Phys. Rev. Lett.* **104**, 100601 (2010).
15. Hsu, C. W., Liew, S. F., Goetschy, A., Cao, H. & Stone, A. D. Correlation-enhanced control of wave focusing in disordered media. *Nat. Phys.* **13**, 497 (2017).
16. Bouchet, D., Rotter, S. & Mosk, A. P. Maximum information states for coherent scattering measurements. *Nat. Phys.* **17**, 564 (2021).
17. Bender, N. et al. Depth-targeted energy delivery deep inside scattering media. *Nat. Phys.* **18**, 309 (2022).
18. Yoon, S. et al. Deep optical imaging within complex scattering media. *Nat. Rev. Phys.* **2**, 141 (2020).
19. Badon, A. et al. Distortion matrix concept for deep optical imaging in scattering media. *Sci. Adv.* **6**, eaay7170 (2020).
20. Yoon, S., Lee, H., Hong, J. H., Lim, Y.-S. & Choi, W. Laser scanning reflection-matrix microscopy for aberration-free imaging through intact mouse skull. *Nat. Commun.* **11**, 5721 (2020).
21. Lambert, W., Cobus, L. A., Frappart, T., Fink, M. & Aubry, A. Distortion matrix approach for ultrasound imaging of random scattering media. *Proc. Natl. Acad. Sci. U.S.A.* **117**, 14645 (2020).
22. Gigan, S. et al. Roadmap on wavefront shaping and deep imaging in complex media. *J. Phys. Photon.* **4**, 042501 (2022).
23. Kang, S. et al. High-resolution adaptive optical imaging within thick scattering media using closed-loop accumulation of single scattering. *Nat. Commun.* **8**, 2157 (2017).
24. Kwon, Y. et al. Computational conjugate adaptive optics microscopy for longitudinal through-skull imaging of cortical myelin. *Nat. Commun.* **14**, 105 (2023).
25. Badon, A., Lerosey, G., Boccara, A. C., Fink, M. & Aubry, A. Retrieving time-dependent Green's functions in optics with low-coherence interferometry. *Phys. Rev. Lett.* **114**, 023901 (2015).
26. Badon, A. et al. Spatio-temporal imaging of light transport in highly scattering media under white light illumination. *Optica* **3**, 1160 (2016).
27. Beaurepaire, E., Boccara, A. C., Lebec, M., Blanchot, L. & Saint-Jalmes, H. Full-field optical coherence microscopy. *Opt. Lett.* **23**, 244 (1998).
28. Dubois, A., Vabre, L., Boccara, A.-C. & Beaurepaire, E. High-resolution full-field optical coherence tomography with a Linnik microscope. *Appl. Opt.* **41**, 805 (2002).
29. Barolle, V. et al. Manifestation of aberrations in full-field optical coherence tomography. *Opt. Express* **29**, 22044 (2021).
30. Mertz, J., Introduction to Optical Microscopy, second edition ed. (Cambridge University Press, Cambridge, United Kingdom ; New York, NY, 2019).
31. Badon, A. et al. Smart optical coherence tomography for ultra-deep imaging through highly scattering media. *Sci. Adv.* **2**, e1600370 (2016).
32. Kang, S. et al. Imaging deep within a scattering medium using collective accumulation of single-scattered waves. *Nat. Photonics* **9**, 253 (2015).
33. Lambert, W., Cobus, L. A., Couade, M., Fink, M. & Aubry, A. Reflection matrix approach for quantitative imaging of scattering media. *Phys. Rev. X* **10**, 021048 (2020).
34. Albada, M. P. V. & Lagendijk, A. Observation of weak localization of light in a random medium. *Phys. Rev. Lett.* **55**, 2692 (1985).
35. Wolf, P.-E. & Maret, G. Weak localization and coherent backscattering of photons in disordered media. *Phys. Rev. Lett.* **55**, 2696 (1985).
36. Goicoechea, A. et al. Reflection measurement of the scattering mean free path at the onset of multiple scattering, https://doi.org/10.48550/arXiv.2401.02246 (2024).
37. Roddier, F., ed. https://doi.org/10.1017/CBO9780511525179 Adaptive Optics in Astronomy (Cambridge University Press, Cambridge, 1999).
38. Judkewitz, B., Horstmeyer, R., Vellekoop, I. M., Papadopoulos, I. N. & Yang, C. Translation correlations in anisotropically scattering media. *Nat. Phys.* **11**, 684 (2015).
39. Osnabrugge, G., Horstmeyer, R., Papadopoulos, I. N., Judkewitz, B. & Vellekoop, I. M. Generalized optical memory effect. *Optica* **4**, 886 (2017).
40. Lambert, W., Cobus, L. A., Robin, J., Fink, M. & Aubry, A. Ultrasound matrix imaging – part II: The distortion matrix for aberration correction over multiple isoplanatic patches. *IEEE Trans. Med. Imag.* **41**, 3921 (2022).
41. Mallart, R. & Fink, M. Adaptive focusing in scattering media through sound?speed inhomogeneities: The van Cittert Zernike approach and focusing criterion. *J. Acoust. Soc. Am.* **96**, 3721 (1994).
42. Wu, T. et al. Single-shot digital optical fluorescence phase conjugation through forward multiple-scattering samples. *Sci. Adv.* **10**, adi1120 (2023).
43. Grieve, K. et al. Stromal striae: a new insight into corneal physiology and mechanics. *Sci. Rep.* **7**, 13584 (2017).
44. Zhu, L. et al. Chromato-axial memory effect through a forward-scattering slab. *Optica* **7**, 338 (2020).
45. Bureau, F. et al. Three-dimensional ultrasound matrix imaging. *Nat. Commun.* **14**, 6793 (2023).
46. Kang, S. et al. Tracing multiple scattering trajectories for deep optical imaging in scattering media. *Nat. Commun.* **14**, 6871 (2023).
47. Jang, M. et al. Relation between speckle decorrelation and optical phase conjugation (OPC)-based turbidity suppression through dynamic scattering media: a study on in vivo mouse skin. *Biomed. Opt. Express* **6**, 72 (2014).
48. Scholler, J. et al. Dynamic full-field optical coherence tomography: 3D live-imaging of retinal organoids. *Light Sci. Appl.* **9**, 140 (2020).
49. Osmanski, B.-F., Montaldo, G., Tanter, M. & Fink, M. Aberration correction by time reversal of moving speckle noise. *IEEE Trans. Ultrason. Ferroelectr. Freq. Control* **59**, 1575 (2012).
50. Campillo, M. & Paul, A. Long-range correlations in the diffuse seismic coda. *Science* **299**, 547 (2003).
51. Labeyrie, A. Attainment of diffraction limited resolution in large telescopes by Fourier analysing speckle patterns in star images. *Astron. Astrophys.* **6**, 85 (1970).
52. Rotter, S. & Gigan, S. Light fields in complex media: Mesoscopic scattering meets wave control. *Rev. Mod. Phys.* **89**, 015005 (2017).
53. Foschini, G. & Gans, M. On limits of wireless communications in a fading environment when using multiple antennas. *Wireless Personal Communications* **6**, 311 (1998).
54. Najar, U. et al. Optical distortion matrices deep inside a human cornea [data]. Zenodo. https://doi.org/10.5281/zenodo.7665117 (2023).

Acknowledgements
The authors wish to thank A. Badon for initial discussions about the experimental set up, K. Irsch for providing the corneal sample and A. Le Ber for providing the iterative phase reversal algorithm. The authors are grateful for the funding provided by the European Research Council (ERC) under the European Union's Horizon 2020 research and innovation program (grant agreement nos. 610110 and 819261, HELMHOLTZ* and REMINISCENCE projects, MF and AA, respectively). This project has also received funding from Labex WIFI (Laboratory of Excellence within the French Program Investments for the Future; ANR-10-LABX-24 and ANR-10-IDEX-0001-02 PSL*, MF).

Author contributions
A.A. initiated and supervised the project. C.B., V.B. and A.A. designed the experimental setup. U.N., V.B. and P.B. built the experimental set up. U.N. and V.B. developed the post-processing tools. U.N. performed the corneal imaging experiment. U.N. and A.A. analyzed the experimental results. V.B. and A.A. performed the theoretical study. A.A. and U.N. prepared the manuscript. U.N., V.B., P.B., M.F., C.B. and A.A. discussed the results and contributed to finalizing the manuscript.

Competing interests
A.A., M.F., C.B. and V.B. are inventors on a patent related to this work held by CNRS (no. US11408723B2, published August 2022). All authors declare that they have no other competing interests.

Additional information
Supplementary information The online version contains supplementary material available at https://doi.org/10.1038/s41467-024-51619-9.

Correspondence and requests for materials should be addressed to Alexandre Aubry.

Peer review information : *Nature Communications* thanks the anonymous reviewer(s) for their contribution to the peer review of this work. A peer review file is available.